Journal of Materials Chemistry C

ROYAL SOCIETY OF CHEMISTRY

PAPER

View Article Online
View Journal | View Issue



Cite this: J. Mater. Chem. C, 2025, 13, 12685

# A metal-free molecular pyroelectric material with strong pyro-photovoltaic coupling for enhancing self-powered X-ray response†

Huaimin Ni,[ab] Haojie Xu,[ab] Aijun Liu,[a] Wuqian Guo,[a] Qingshun Fan,[ab] Yi Liu,*[a] Zihao Zhao,[ab] Xianmei Zhao,[a] Junhua Luo [abc] and Zhihua Sun *[abc]

Metal-free X-ray detectors have shown enormous application potential in the fields of public safety and medical diagnostics owing to their environmentally sustainable and low-cost characteristics. However, the X-ray absorption and response capabilities of metal-free materials are constrained by their intrinsic low atomic number and low density. Here, we have constructed a series of metal-free pyroelectric materials, **CY–X** (CY = cyclohexylamine, X = Cl, Br, and I), showing remarkable X-ray detection responses enabled by the pyro-photovoltaic coupling effect. Interestingly, benefiting from the molecule-level modification, the pyroelectric-active candidate **CY–I** exhibits a high pyroelectric coefficient $P_e$ of $\sim 35 \times 10^{-4}$ μC cm$^{-2}$ K$^{-1}$ and demonstrates an exceptional photo-pyroelectric effect across a broad spectrum, covering the range from X-ray to 266–980 nm. Such X-ray-response pyro-photovoltaic coupling behavior enables a significant improvement in the photocurrent (~158.5%), facilitating superior self-powered X-ray detection, including sensitivity (88 μC Gy$^{-1}$ cm$^{-2}$) and a low detection limit (137 nGy s$^{-1}$). This work provides an effective solution to enhance the X-ray response performance in metal-free materials and offers new insights into the development of environmentally friendly, self-powered broadband detectors.

Received 24th March 2025,
Accepted 9th May 2025

DOI: 10.1039/d5tc01275a

rsc.li/materials-c



## 1. Introduction

X-ray photons have been extensively utilized in medical treatment, industrial defect detection, public safety, and scientific research attributed to their excellent penetrating ability.[1–4] Currently, most commercial X-ray detectors are inorganic materials, such as Si,[5] CdTe,[6] and amorphous Se,[7] which exhibit excellent X-ray imaging capabilities and response characteristics. Although this type of detector dominates in X-ray detection,[8–11] it suffers from several limitations, including high manufacturing costs, toxicity, and low mechanical flexibility.[12–15] In context, metal-free materials have emerged as a promising alternative or supplement for the development of X-ray detectors owing to their environmental friendliness, low cost, and high flexibility.[16,17] For example, an X-ray detector fabricated by blending Se-containing $P_3HSe$ with $PC_{70}BM$ exhibits a sensitivity of 600 ± 11 nC Gy$^{-1}$ cm$^{-2}$.[18] Besides, the 2 × 2-pixel X-ray detector based on a flexible TIPS–pentacene organic thin film achieves light response to X-ray radiation at a low applied voltage of 0.2 $V_{bias}$, with a sensitivity of up to 77 000 nC mGy$^{-1}$ cm$^{-2}$.[19] Despite appreciable progress having been achieved in the application of metal-free materials for X-ray detection, several critical challenges hinder their practical implementation, including complex molecular engineering, environmental instability, and high energy consumption.[20–22] Additionally, the low $Z$ and densities of metal-free materials severely limit their X-ray absorption ability and photocurrent response.[23,24] Therefore, it is crucial to develop self-powered metal-free X-ray detectors and improve their X-ray photocurrent response.

The photo-pyroelectric effect refers to a physical phenomenon wherein thermal radiation from laser excitation induces thermal changes in electric dipoles. This change further triggers carrier redistribution and generates a measurable electrical signal within the material.[25,26] Notably, this process is primarily driven by the pyroelectric effect rather than the photoelectric effect, thereby overcoming the limitations imposed by the optical bandgap (non-ionizing radiation within the UV-NIR spectral region). The feature highlights the potential of pyroelectric materials for self-powered broadband detection applications. For example, the pyroelectric material (*N*,*N*-dimethylcyclohexylammonium)$PbBr_3$ achieves full spectral region response ranging from 266 nm to 1950 nm through the photo-pyroelectric effect, providing a novel approach

[a] State Key Laboratory of Functional Crystals and Devices Fujian Institute of Research on the Structure of Matter Chinese Academy of Sciences Fuzhou, Fujian 350002, P. R. China. E-mail: sunzhihua@fjirsm.ac.cn
[b] University of Chinese Academy of Sciences Beijing, 100049, P. R. China
[c] Fujian Science & Technology Innovation Laboratory for Optoelectronic Information of China Fuzhou, Fujian, 350108, P. R. China

† Electronic supplementary information (ESI) available. CCDC 2430249–2430251. For ESI and crystallographic data in CIF or other electronic format see DOI: https://doi.org/10.1039/d5tc01275a

for driving broadband photoactivity.[27] Furthermore, as an effective strategy for regulating charge carrier behavior, the photo-pyroelectric effect can realize dual-channel modulation through synergistic coupling with the photovoltaic effect.[28,29] This pyro-photovoltaic coupling effect can be achieved across a broad spectral range, extending from the visible light spectrum to the X-ray region, as demonstrated in materials such as (2,4-difluorobenzylamine)$_2$PbCl$_4$ and (neopentylammonium)$_4$AgBiBr$_8$.[30,31] In context, introducing the pyroelectric–photovoltaic coupling effect into metal-free pyroelectric material systems offers a promising solution to overcome their inherent constraints in X-ray absorption and photocurrent response.

In this work, we have synthesized a series of metal-free pyroelectric materials, **CY–X** (where CY = cyclohexylamine, X = Cl, Br, and I). The modification of the halogen bond improves the pyroelectric performance of **CY–X**. Notably, **CY–I** exhibits a high pyroelectric coefficient ($P_e = 35 \times 10^{-4}$ μC cm$^{-2}$ K$^{-1}$), representing an approximately 310% enhancement compared to that of **CY–Cl**. Based on its superior pyroelectric properties, **CY–I** shows a unique pyro-photovoltaic coupling effect under X-ray irradiation, which causes a remarkable improvement in photocurrent response of ~158.5%. Strikingly, this pyro-photovoltaic coupling effect enables excellent self-powered X-ray detection performance, including a sensitivity of 88 μC Gy$^{-1}$ cm$^{-2}$ and a low detection limit of 137 nGy s$^{-1}$. Therefore, this work establishes an effective strategy for developing high-performance X-ray detectors based on metal-free materials.

## 2. Experimental section

### 2.1. Materials and bulk crystal growth

All chemical reagents and solvents were purchased and employed without further purification. Colorless, large crystals were obtained by evaporating mixed solutions of cyclohexylamine with stoichiometric hydrogen chloride, hydrogen bromide, and hydrogen iodide. The solutions were prepared using a 1 : 1 (v/v) mixture of ethanol and distilled water and then subjected to evaporation in an oven set at 45 °C for 10 days.

### 2.2. Preparation of electrodes

For photoelectric characterization, we selected a high-quality single crystal (0.5 × 1.5 × 3 mm$^3$) exhibiting regular morphology and minimal structural defects. Planar electrodes were fabricated by uniformly coating both crystal termini with conductive silver paste of equal surface area, maintaining an interelectrode spacing of approximately 3 mm.

### 2.3. Single-crystal X-ray crystallography and powder X-ray diffraction

A Bruker D8 diffractometer with Mo Kα radiation ($\lambda$ = 0.71073) was used for single-crystal X-ray diffraction at 230 K. APEX3 software was used for data reduction, and SHELXLTL software was employed for crystal structure solution and refinement. The PXRD pattern was collected with a scan rate of 5° min$^{-1}$ in the 2-theta ($2\theta$) range of 5°–40°.

### 2.4. Physical property measurements

The second harmonic generation (SHG) measurements were performed using an FLS 920 spectrometer equipped with a Vibrant 355 II OPO laser operating at the fundamental wavelength of 1064 nm. Thermogravimetric measurement was carried out using an STA449C thermal analyzer in the range of 300–1200 K.

### 2.5. Photoresponse measurements

A Keithley 2636B electrometer was used to measure the output current. The dynamic pyroelectric current was obtained at room temperature using the Chynoweth technique. THORLABS 404, 520, 637, 785, and 980 nm pigtailed laser diodes were used for visible light illumination. A homemade 266 nm laser (LDMQ-266-10) was used for ultraviolet light illumination.

The pyroelectric coefficient ($P_e$) of **CY–X** (X = Cl, Br, and I) was calculated using the following equations:

$$i_A = A\frac{dP_s}{dt} = A\frac{dP_s}{dT}\frac{dT}{dt} = AP_e\frac{dT}{dt}$$

$$P_e = \frac{\int i_A dt}{A\Delta T} = \frac{\Delta S}{\Delta T}$$

In the equation $P_e = dP_s/dt$, where $i_A$, $A$, $P_s$, $t$, $T$, and $S$ denote the pyroelectric current, the effective area between the electrodes, spontaneous polarization, time, temperature, and charge density, respectively.

### 2.6. X-Ray detection

The X-ray detection instrument was an Amptek MiniX tube with a silver target and a maximum power output of 4 W. The X-ray source was calibrated using a silicon detector, generating continuous X-rays with energies up to 50 keV and an average energy of 22 keV.

The signal-to-noise ratio (SNR) was calculated using the following equations:

$$SNR = \frac{(I_{photo} - I_{dark})}{\sqrt{\frac{1}{N}\sum_{i}^{n}(I_i - I_{photo})^2}}$$

where $I_i$, $I_{photo}$, and $I_{dark}$ represent the photocurrent, average photocurrent, and average dark current under X-ray irradiation, respectively.

## 3. Results and discussion

### 3.1. Crystal characterization

The crystals of **CY–X** (where CY = cyclohexylamine, X = Cl, Br, and I) were obtained by slowly evaporating a mixed solution of ethanol and distilled water in equal volume ratios. The phase purity of **CY–X** was confirmed by powder X-ray diffraction (PXRD). The results show that the PXRD pattern of the fresh crystal of **CY–I** is fairly consistent with that of the crystal that was exposed to the ambient atmosphere for 90 days, which confirms the long-term phase stability (Fig. S1, ESI†). The thermal stability of **CY–X**

 

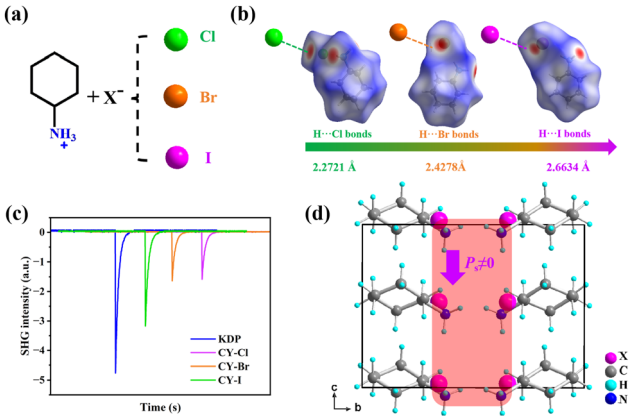


Fig. 1 (a) Crystal structures of **CY–X**. (b) Hydrogen bond lengths under different halogen ions of **CY–X**. (c) SHG intensity of **CY–X** and KDP at room temperature ($\lambda$ = 1064 nm). (d) Stacking structure and spontaneous polarization orientation of **CY–X**.

was confirmed by thermogravimetric analysis (TG) (Fig. S2, ESI†). The crystal structure analysis indicates that the basic unit of **CY–X** is a hydrogen bond dimer (Fig. 1a), which is composed of cyclohexylamine and halogen through N–H···X hydrogen bonds (Fig. 1b). The two-dimensional fingerprint also reveals the strong hydrogen bond interaction on the Hirshfeld surface (Fig. S3, ESI†). In detail, the **CY–X** all belong to the polar space group $Pca2_1$ (Fig. S4, ESI†), and the second harmonic generation (SHG) response confirms the non-centrosymmetric structural characteristics of **CY–X** (Fig. 1c). From the perspective of crystal structure, the spatial ordering of cations and anions plays a crucial role in inducing polarization in materials. This ordered arrangement facilitates the directional alignment of intrinsic dipole moments within the crystal lattice, ultimately resulting in non-zero net polarization vectors along the crystallographic *c*-axis (Fig. 1d).[32] Therefore, the structural characteristics of **CY–X** provide significant potential for the realization of intrinsic polarity and an exceptional pyroelectric effect. Notably, the increase in halogen atom radius leads to a decrease in electronegativity during halogen substitution from $Cl^-$ to $I^-$. The electron cloud distribution of low electronegativity $I^-$ is more diffuse, which promotes an increase in the N–H···I hydrogen bonds (N–H···Cl: 2.2721 Å, N–H···Br: 2.4278 Å, N–H···I: 2.6634 Å). These results enable a greater distance between the positive and negative charge centers in **CY–I**, which in turn expands the length of the dipole moment. Therefore, **CY–I** exhibits a larger molecular dipole moment and spontaneous polarization strength, which has been verified by the structure–activity relationship of the molecular ferroelectric system.[33,34]

### 3.2. Pyroelectric properties

To confirm the pyroelectric properties of **CY–X**, the electrodes were prepared along the polar axis (*c*-axis) of the crystal. The pyroelectric properties of **CY–X** were characterized using the dynamic method. A 404 nm laser with a power density of 100 mW $cm^{-2}$ was used as the incident source. Under periodic optical radiation switching, a temperature fluctuation of 0.5 K was observed on the crystal surface (Fig. S5, ESI†). This transient temperature variation induces a pronounced pyroelectric current, confirming the pyroelectric properties of **CY–X** (Fig. 2a–c). Interestingly, the pyroelectric properties of **CY–X** can be effectively tuned through Cl/Br/I halogen modification. In detail, the pyroelectric coefficient ($P_e$) increases by approximately 310% (Fig. S6, ESI†), ranging from 11.3 × $10^{-4}$ μC $cm^{-2}$ $K^{-1}$ in **CY–Cl** to 35 × $10^{-4}$ μC $cm^{-2}$ $K^{-1}$ in **CY–I**. This $P_e$ value is comparable to those of conventional pyroelectric materials, such as $BiFeO_3$ (30 × $10^{-4}$ μC $cm^{-2}$ $K^{-1}$) and PVDF (27 × $10^{-4}$ μC $cm^{-2}$ $K^{-1}$) (Fig. 2d).[35] The results reveal the feasibility of halogen modification strategies for optimizing pyroelectric properties.

### 3.3. Broadband response from UV-NIR

As expected, **CY–I** exhibits excellent sensitivity to minor temperature changes and generates significant pyroelectric currents under laser-induced thermal irradiation (Fig. 3a). Specifically, the instantaneous laser irradiation raises the surface temperature of the crystal, thereby disrupting the balance of dipoles within the crystal. This process leads to the change in surface polarization, producing a positive pyroelectric current. As laser irradiation persists, the temperature of the crystal surface gradually reaches thermal equilibrium. During this process, the distribution of the electric dipole moment inside the crystal rebalances, causing the return of the current to the dark state level. Furthermore, when laser radiation is turned off, the crystal surface temperature sharply declines. This temperature variation disrupts the dipole equilibrium within the crystal once again, which leads to the generation of a reverse pyroelectric current. As the temperature stabilizes, the current eventually returns to its dark current state (Fig. S7, ESI†).[36,37] As shown in Fig. 3b and c, **CY–I** exhibits pronounced photo-pyroelectric response characteristics, with an effective response range spanning from 266 to 980 nm. This mechanism of broadband response is independent of the optical bandgap. Notably, the pyroelectric current exhibits an obvious increase with increasing light power density under 785 nm laser illumination (Fig. 3d). This enhancement can be attributed to the greater temperature fluctuations induced by higher light intensity, which promotes the

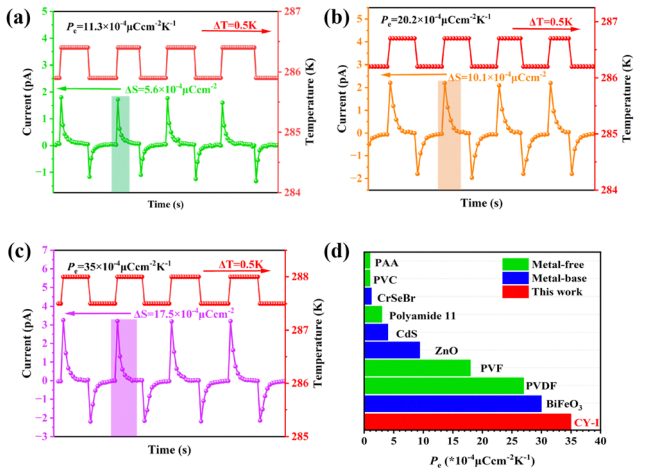


Fig. 2 Pyroelectric coefficients of **CY–X**: (a) **CY–Cl**, (b) **CY–Br**, and (c) **CY–I**. (d) Comparison of the $P_e$ of various reported pyroelectric materials.

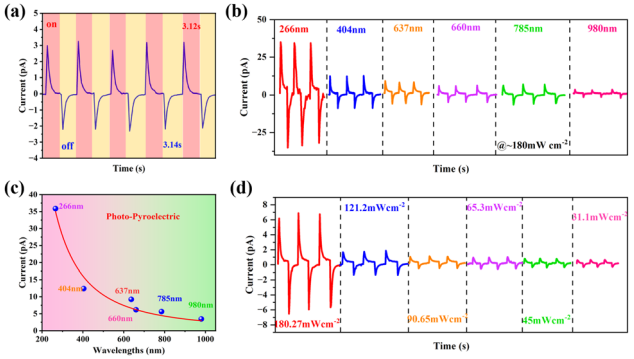


Fig. 3 (a) Light response cycles and the corresponding response time. (b) Pyroelectric-induced photodetection behavior and (c) pyroelectric current values of **CY–I** under 266–980 nm laser irradiation (180 mW $cm^{-2}$, at 0 $V_{bias}$). (d) Photodetection behavior of **CY–I** under 785 nm laser irradiation at different power densities (at 0 $V_{bias}$).

generation of charge carriers. The results highlight the application potential of metal-free molecular pyroelectric materials in self-powered broadband detection.

### 3.4. X-ray band response

Interestingly, **CY–I** exhibits a significant pyro-photovoltaic coupling effect under X-ray irradiation, revealing its ability to achieve dual-channel modulation of X-ray-induced carriers through distinct physical mechanisms. This finding provides a solution to the challenge of poor X-ray response in metal-free materials, which typically arises from their intrinsically low atomic number ($Z$) and low density. Notably, the X-ray attenuation coefficient and absorption of **CY–I** are higher than those of HCB,[38] TIPS–pentacene, and DABCO–$NH_4Cl_3$[39] (Fig. S8a and b, ESI†). The high attenuation efficiency indicates that **CY–I** has a strong capability to generate photogenerated carriers under X-ray irradiation. As shown in Fig. 4a, **CY–I** exhibits a high bulk resistivity ($\rho$ = 5.2 × $10^{12}$ Ω cm), which effectively suppresses the dark current and thus enables sensitive X-ray response. Furthermore, the $\mu\tau$ product serves as a critical performance merit for high-performance X-ray detectors. By fitting the modified Hecht equation of **CY–I**, an excellent $\mu\tau$ product of approximately 1.3 × $10^{-3}$ $cm^2$ $V^{-1}$ was determined (Fig. 4b). This $\mu\tau$ product significantly surpasses those of Pb-based perovskites, such as $(S\text{-BPEA})_2FAPb_2I_7$

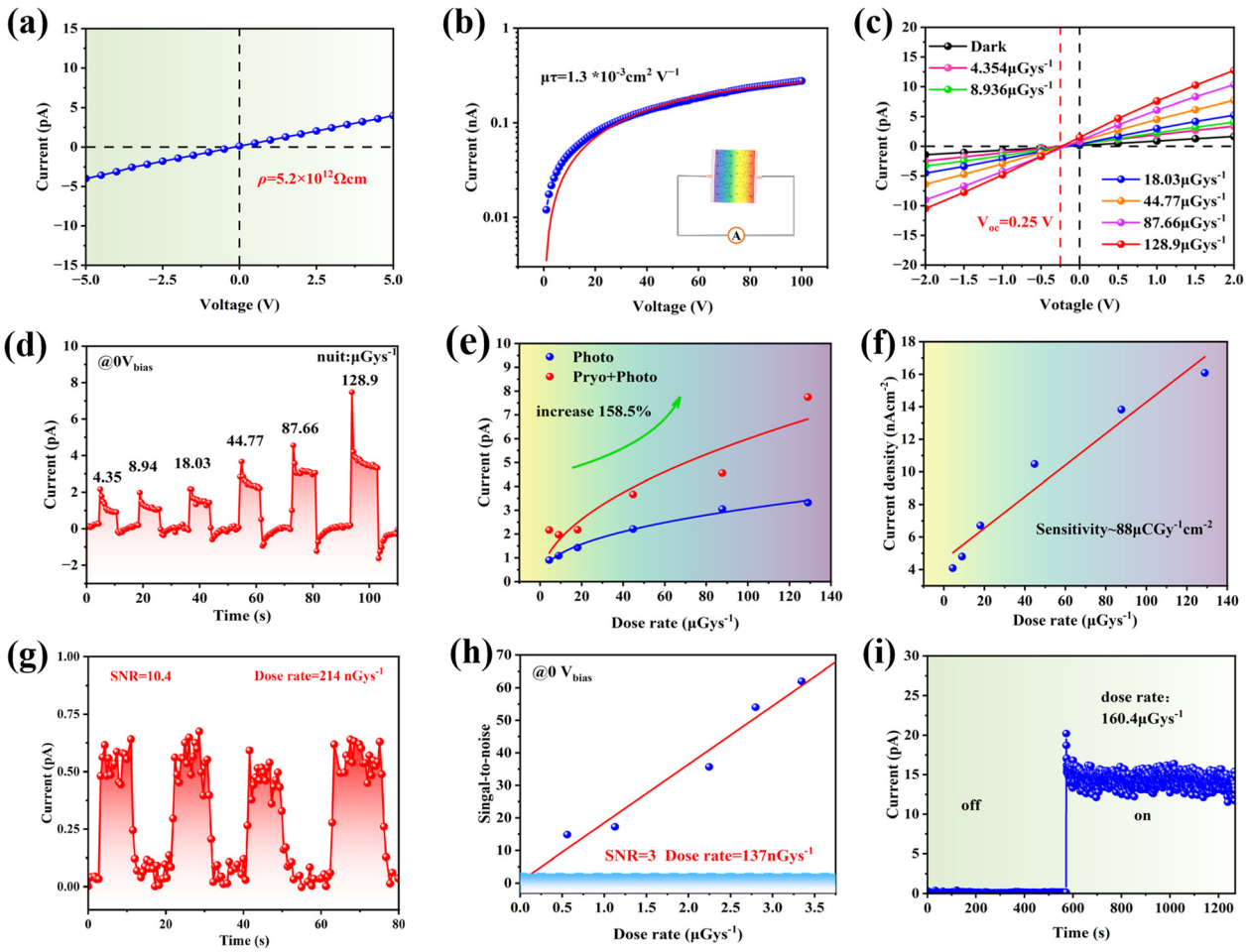


Fig. 4 X-ray detection performance of **CY–I**. (a) Bulk resistivity measurement. (b) The $\mu\tau$ product (inset: The single crystal device). (c) $I$–$V$ curves showing a BPVE under X-ray irradiation. (d) Photocurrent under different dose rates at 0 $V_{bias}$. (e) $I_{photo}$ and $I_{pyro+photo}$ under different dose rates. (f) Sensitivity at 0 $V_{bias}$. (g) $I$–$t$ curves and the calculated SNR under X-ray irradiation at 0 $V_{bias}$. (h) SNR under different dose rates at 0 $V_{bias}$. (i) Photocurrent stability under continuous X-ray irradiation at 0 $V_{bias}$.

($1.6 \times 10^{-4}$ $cm^2$ $V^{-1}$) and $(NH_3C_4H_8NH_3)PbI_4$ ($4.43 \times 10^{-4}$ $cm^2$ $V^{-1}$).[40,41] At 10 $V_{bias}$, the dark current drift ($I_{drift}$) value of **CY–I** is as low as $8.2 \times 10^{-7}$ nA $cm^{-1}$ $s^{-1}$ $V^{-1}$, indicating low-level ion migration in **CY–I** (Fig. S9, ESI†).

Due to the high sensitivity of this device to temperature fluctuations, the X-ray detection performance was tested under stable environmental conditions. The *I–V* curves at different X-ray radiation dose rates were measured. As shown in Fig. 4c, a bulk photovoltaic effect (BPVE) was observed, with an open-circuit voltage of 0.25 V being measured. Especially, a pyroelectric current signal can be induced under X-ray irradiation at 0 $V_{bias}$, and the current intensity shows a positive correlation with the dose rate. The instantaneous X-ray radiation raises the surface temperature of the crystal (Fig. S10, ESI†), thereby disrupting the equilibrium of the dipole within the crystal. This process leads to a change in surface polarization, resulting in a positive pulsed pyroelectric current. With the increase in the X-ray dose rate, the temperature variation on the crystal surface becomes more pronounced. The pulsed current generated by this device exhibits a response characteristic highly consistent with that induced by laser irradiation with wavelengths below the **CY–I** bandgap. When the X-ray radiation is turned off, the current decay profile in Fig. 4d displays a distinct reverse pyroelectric peak characteristic induced by the abrupt temperature drop, which fundamentally differs from the slow tailing attenuation reported in the literature. These results provide conclusive evidence that the pulsed current originates predominantly from the pyroelectric effect.[42] Strikingly, based on the pyro-photovoltaic coupling effect, **CY–I** realizes photocurrent boosting with a maximum contrast of ~158.5% (Fig. 4e) and exhibits excellent self-powered X-ray detection performance. By fitting the curves between current density and the dose rate at 0 $V_{bias}$, a sensitivity of 88 μC $Gy^{-1}$ $cm^{-2}$ is obtained (Fig. 4f). As shown in Fig. S12 (ESI†), **CY–I** exhibits photoresponse times of 0.531 s (raise time) and 0.516 s (decay time) during a single switching cycle. Low detection limits are critical for estimating the effectiveness of X-ray detectors in practical applications. As shown in Fig. 4g, the signal-to-noise ratio (SNR) for **CY–I** is 10.4 at a low dose of 214 nGy $s^{-1}$. Additionally, by fitting the SNR to the dose rate and dependency curve, the result shows that the calculated X-ray detection limit of **CY–I** is approximately 137 nGy $s^{-1}$ at an SNR of 3, which is significantly lower than the typical dose rate in medical X-ray diagnostics (5.5 μGy $s^{-1}$) (Fig. 4h). Such a low detection limit reduces the biological hazard in the X-ray detection process.[43–45] As shown in Fig. 4i, the device exhibits excellent operational stability under high dose rate conditions. After continuous exposure to X-ray radiation for up to 10 minutes at 0 $V_{bias}$, the photocurrent output of the device remains stable, indicating a higher practical level of **CY–I**.[46] Therefore, this work offers a feasible solution to the challenge of achieving strong X-ray responses in metal-free materials.

## 4. Conclusions

In summary, we have reported a series of metal-free pyroelectric materials, **CY–X** (X = Cl, Br, and I), through a subtle molecule-level modification. Among these pyroelectrics, **CY–I** achieves the highest pyroelectric coefficient ($P_e = 35 \times 10^{-4}$ μC $cm^{-2}$ $K^{-1}$). It demonstrates an exceptional photo-pyroelectric effect across a broad spectral range, from X-ray to 266–980 nm. Based on the X-ray-induced pyro-photovoltaic coupling effect, **CY–I** exhibits a photocurrent enhancement with a maximum contrast of ~158.5%. Moreover, it achieves superior self-powered X-ray detection performance, including sensitivity (88 μC $Gy^{-1}$ $cm^{-2}$) and a low detection limit (137 nGy $s^{-1}$). Therefore, this work provides an effective methodology for improving X-ray response performance in metal-free materials.

## Author contributions

H. Ni synthesized and characterized the pyroelectric materials. H. Xu determined the single-crystal structure. A. Liu performed the calculation and analysis. W. Guo, Q. Fan, Z. Zhao, and X. Zhao conducted the characterization of the detector device. J. Luo provided suggestions for research. Z. Sun and Y. Liu designed and directed the studies. H. Ni and Z. Sun wrote the manuscript. All authors discussed the results and reviewed the manuscript.

## Data availability

CCDC 2430249–2430251† contains the crystallographic data in this paper, which can be obtained free of charge from **https://www.ccdc.cam.ac.uk/**. All other relevant data generated and analysed during this study, which include experimental, crystallographic and computational data, are included in this article and its ESI.†

## Conflicts of interest

There are no conflicts to declare.

## Acknowledgements

This work was supported by the NSFC (22125110, U23A2094, 22205233, 22193042, 21921001, 22305248, and U21A2069), the Natural Science Foundation of Fujian Province (2023J02028), the Key Research Program of Frontier Sciences of Chinese Academy of Sciences (ZDBS-LY-SLH024), Fujian Science & Technology Innovation Laboratory for Optoelectronic Information of China (2021ZR126), and the National Key Research and Development Program of China (2019YFA0210402).

## Notes and references

1 Y. C. Kim, K. H. Kim, D.-Y. Son, D.-N. Jeong, J.-Y. Seo, Y. S. Choi, I. T. Han, S. Y. Lee and N.-G. Park, *Nature*, 2017, **550**, 87–91.
2 X. Li, G. Zhang, Y. Hua, X. Sun, J. Liu, H. Liu, Z. Yue, Z. Zhai, H. Xia and X. Tao, *J. Mater. Chem. C*, 2024, **12**, 10613–10620.

3 J.-X. Wang, L. Gutiérrez-Arzaluz, X. Wang, T. He, Y. Zhang, M. Eddaoudi, O. M. Bakr and O. F. Mohammed, *Nat. Photonics*, 2022, **16**, 869–875.
4 B. Xiao, Q. Sun, F. Wang, S. Wang, B.-B. Zhang, J. Wang, W. Jie, P. Sellin and Y. Xu, *J. Mater. Chem. A*, 2021, **9**, 13209–13219.
5 M. J. Yaffe and J. A. Rowlands, *Phys. Med. Biol.*, 1997, **42**, 1–39.
6 K. M. Oh, D. K. kim, J. W. Shin, S. U. Heo, J. S. Kim, J. G. Park and S. H. Nam, *J. Instrum.*, 2014, **9**, P01010.
7 S. O. Kasap, *J. Phys. D: Appl. Phys.*, 2000, **33**, 2853.
8 C. Szeles, *Phys. Status Solidi B*, 2004, **241**, 783–790.
9 H. Wei and J. Huang, *Nat. Commun.*, 2019, **10**, 1066.
10 X. Geng, Y. A. Chen, Y. Y. Li, J. Ren, G. H. Dun, K. Qin, Z. Lin, J. Peng, H. Tian, Y. Yang, D. Xie and T. L. Ren, *Adv. Sci.*, 2023, **10**, 2300256.
11 W. Ning, F. Wang, B. Wu, J. Lu, Z. Yan, X. Liu, Y. Tao, J. M. Liu, W. Huang, M. Fahlman, L. Hultman, T. C. Sum and F. Gao, *Adv. Mater.*, 2018, **30**, 1706246.
12 Y. Li, W. Shi, A. Gupta and N. Chopra, *RSC Adv.*, 2015, **5**, 49708–49718.
13 M. Chen, C. Wang and W. Hu, *J. Mater. Chem. C*, 2021, **9**, 4709–4729.
14 S. Zhao, J. Wu, K. Jin, H. Ding, T. Li, C. Wu, N. Pan and X. Wang, *Adv. Funct. Mater.*, 2018, **28**, 1802011.
15 R. Saran and R. J. Curry, *Nat. Photonics*, 2016, **10**, 81–92.
16 H. Xu, W. Guo, Y. Ma, Y. Liu, X. Hu, L. Hua, S. Han, X. Liu, J. Luo and Z. Sun, *Nat. Commun.*, 2022, **13**, 5329.
17 H. Dong, H. Zhu, Q. Meng, X. Gong and W. Hu, *Chem. Soc. Rev.*, 2012, **41**, 1754–1808.
18 M. P. A. Nanayakkara, Q. He, A. Ruseckas, A. Karalasingam, L. Matjacic, M. G. Masteghin, L. Basiricò, I. Fratelli, A. Ciavatti, R. C. Kilbride, S. Jenatsch, A. J. Parnell, B. Fraboni, A. Nisbet, M. Heeney, K. D. G. I. Jayawardena and S. R. P. Silva, *Adv. Sci.*, 2023, **10**, 2304261.
19 L. Basiricò, A. Ciavatti, T. Cramer, P. Cosseddu, A. Bonfiglio and B. Fraboni, *Nat. Commun.*, 2016, **7**, 13063.
20 A. Ciavatti, E. Capria, A. Fraleoni-Morgera, G. Tromba, D. Dreossi, P. J. Sellin, P. Cosseddu, A. Bonfiglio and B. Fraboni, *Adv. Mater.*, 2015, **27**, 7213–7220.
21 A. D. Scaccabarozzi, A. Basu, F. Aniés, J. Liu, O. Zapata-Arteaga, R. Warren, Y. Firdaus, M. I. Nugraha, Y. Lin, M. Campoy-Quiles, N. Koch, C. Müller, L. Tsetseris, M. Heeney and T. D. Anthopoulos, *Chem. Rev.*, 2021, **122**, 4420–4492.
22 W. Guo, H. Xu, Y. Ma, Y. Liu, H. Gao, T. Hu, W. Ren, J. Luo and Z. Sun, *Angew. Chem., Int. Ed.*, 2023, **62**, e202300028.
23 X. Wang, H. Shi, H. Ma, W. Ye, L. Song, J. Zan, X. Yao, X. Ou, G. Yang, Z. Zhao, M. Singh, C. Lin, H. Wang, W. Jia, Q. Wang, J. Zhi, C. Dong, X. Jiang, Y. Tang, X. Xie, Y. Yang, J. Wang, Q. Chen, Y. Wang, H. Yang, G. Zhang, Z. An, X. Liu and W. Huang, *Nat. Photonics*, 2021, **15**, 187–192.
24 D. Zhao, R. Gao, W. Cheng, M. Wen, X. Zhang, T. Yokota, P. Sellin, S. A. Yang, L. Shang, C. Zhou, T. Someya, W. Jie and Y. Xu, *Nat. Commun.*, 2024, **15**, 1115.
25 J. Tian, *AIP Adv.*, 2023, **13**, 050701.
26 L. Wang, F. Zhang, C. Chen, X. He, M. A. Boda, K. Yao and Z. Yi, *Nano Energy*, 2024, **119**, 109081.
27 W. Guo, H. Xu, W. Weng, L. Tang, Y. Ma, Y. Liu, L. Hua, B. Wang, J. Luo and Z. Sun, *Angew. Chem., Int. Ed.*, 2022, **61**, e202213477.
28 Y. Liu, X. Pan, X. Liu, S. Han, J. Wang, L. Lu, H. Xu, Z. Sun and J. Luo, *Small*, 2022, **18**, 2106888.
29 W. Li, Y. Ma, Y. Liu, Q. Fan, H. Xu, W. Guo, L. Tang, H. Rong, Z. Sun and J. Luo, *Angew. Chem., Int. Ed.*, 2025, **64**, e202417036.
30 X. Zeng, Y. Liu, Y. Chen, Q. Fan, T. Yang, L. Tang, W. Guo, Y. Ma, J. Luo and Z. Sun, *ACS Energy Lett.*, 2024, **9**, 381–387.
31 W. Li, Y. Ma, Y. Liu, Q. Fan, H. Xu, W. Guo, L. Tang, H. Rong, Z. Sun and J. Luo, *Angew. Chem., Int. Ed.*, 2025, **64**, e202417036.
32 L. Mao, C. C. Stoumpos and M. G. Kanatzidis, *J. Am. Chem. Soc.*, 2019, **141**, 1171–1190.
33 R. K. Saripalli, D. Swain, S. Prasad, H. Nhalil, H. L. Bhat, T. N. Guru Row and S. Elizabeth, *J. Appl. Phys.*, 2017, **121**, 114101.
34 D.-W. Fu, H.-L. Cai, Y. Liu, Q. Ye, W. Zhang, Y. Zhang, X.-Y. Chen, G. Giovannetti, M. Capone, J. Li and R.-G. Xiong, *Science*, 2013, **339**, 425–428.
35 R. Mondal, M. A. M. Hasan, J. M. Baik and Y. Yang, *Mater. Today*, 2023, **66**, 273–301.
36 V. Panwar, S. Nandi, M. Majumder and A. Misra, *J. Mater. Chem. C*, 2022, **10**, 12487–12510.
37 X. Zeng, Y. Liu, W. Weng, L. Hua, L. Tang, W. Guo, Y. Chen, T. Yang, H. Xu, J. Luo and Z. Sun, *Nat. Commun.*, 2023, **14**, 5821.
38 D. Zhao, M. Xu, B. Xiao, B. Zhang, L. Yan, G. Zeng, A. Dubois, P. Sellin, W. Jie and Y. Xu, *J. Mater. Chem. A*, 2020, **8**, 5217–5226.
39 Q. Cui, X. Song, Y. Liu, Z. Xu, H. Ye, Z. Yang, K. Zhao and S. Liu, *Matter*, 2021, **4**, 2490–2507.
40 Q. Guan, H. Ye, S. You, Z. K. Zhu, H. Li, X. Liu and J. Luo, *Small*, 2023, **20**, 2307908.
41 Y. Shen, Y. Liu, H. Ye, Y. Zheng, Q. Wei, Y. Xia, Y. Chen, K. Zhao, W. Huang and S. Liu, *Angew. Chem., Int. Ed.*, 2020, **59**, 14896–14902.
42 Z. Wang, R. Yu, C. Pan, Z. Li, J. Yang, F. Yi and Z. L. Wang, *Nat. Commun.*, 2015, **6**, 8401.
43 M. P. A. Nanayakkara, L. Matjačić, S. Wood, F. Richheimer, F. A. Castro, S. Jenatsch, S. Züfle, R. Kilbride, A. J. Parnell, M. G. Masteghin, H. M. Thirimanne, A. Nisbet, K. D. G. I. Jayawardena and S. R. P. Silva, *Adv. Funct. Mater.*, 2020, **31**, 2008482.
44 Z. Li, Z. Li, G. Peng, C. Shi, H. Wang, S. Y. Ding, Q. Wang, Z. Liu and Z. Jin, *Adv. Mater.*, 2023, **35**, 2300480.
45 Y. Zhang, Y. Liu, Z. Xu, H. Ye, Z. Yang, J. You, M. Liu, Y. He, M. G. Kanatzidis and S. Liu, *Nat. Commun.*, 2020, **11**, 2304.
46 M. Girolami, F. Matteocci, S. Pettinato, V. Serpente, E. Bolli, B. Paci, A. Generosi, S. Salvatori, A. Di Carlo and D. M. Trucchi, *Nano-Micro Lett.*, 2024, **16**, 182.

 